Modeling of ALOS and COSMO-SkyMed satellite data at Mt Etna: implications on relation between seismic activation of the Pernicana fault system and volcanic unrest

Gilda Currenti[1], Giuseppe Solaro[2], Rosalba Napoli[1], Antonio Pepe[2], Alessandro Bonaccorso[1], Ciro Del Negro[1], Eugenio Sansosti[2]

[1] *Istituto Nazionale di Geofisica e Vulcanologia – Sezione di Catania, Osservatorio Etneo, Catania, Italy*

[2] *National Research Council (CNR) – Istituto per il Rilevamento Elettromagnetico dell'Ambiente (IREA), Napoli, Italy*

Abstract

We investigate the displacement induced by the 2-3 April 2010 seismic swarm (the largest event being of Ml 4.3 magnitude) by means of InSAR data acquired over the volcano by the Cosmo-SkyMed and ALOS radar systems. Satellite observations, combined with leveling data, allowed us to perform a high-resolution modeling inversion capable of fully capturing the deformation pattern and identifying the mechanism responsible for the PFS seismic activation. The inversion results well explain high gradients in the radar line of sight displacements observed along the fault rupture. The slip distribution model indicates that the fault was characterized by a prevailing left-lateral and normal dip-slip motion with no fault dilation and, hence, excludes that the April 2010 seismic swarm is a response to accommodate the stress change induced by magma intrusions, but it is due to the tectonic loading possibly associated with sliding of the eastern flank of the volcano edifice. These results provide a completely different scenario from that derived for the 22 September 2002 M3.7 earthquake along the PFS, where the co-seismic shear-rupture was accompanied by a tensile mechanism associated with a first attempt of magma intrusion that preceded the lateral eruption occurred here a month later. These two opposite cases provide hints into the behavior of the PFS between quiescence and unrest periods at Etna and pose different implications for eruptive activity prediction and volcano hazard assessment. The dense pattern of ground deformation provided by integration of data from short revisiting time satellite missions, together with refined modeling for fault slip distribution, can be exploited at different volcanic sites, where the activity is controlled by volcano-tectonic interaction processes, for a timely evaluation of the impending hazards.

Key-words: Etna volcano, ground deformation, satellite interferometry, source modeling.

1. Introduction

Eruptive sequences and local seismicity on Etna volcano have often revealed a significant temporal correlation between the occurrence of large earthquakes along the main volcano-tectonic structures and periods of volcanic unrest. In the Etna northern flank, one of the most intriguing volcano-tectonic structures is the Pernicana Fault System (PFS), which have been showing a controversial relationship between seismic activation and volcanic unrest over the last decades. The PFS is characterized both by aseismic continuous "slow" movements associated with the sliding of the Mt Etna eastern flank (Azzaro et al., 2001; Ruch et al., 2010) and by shallow earthquakes causing surface ruptures and severe damages to man-made infrastructures in the surrounding area (Bonforte et al., 2007; Currenti et al., 2010). Several times the seismic energy release has preceded the onset of lateral eruptions in the Etna northern flank.

The 22 September 2002 M3.7 event represents an exemplary case, in which the seismic release preceded by nearly a month the violent and dramatic explosive-effusive flank eruption of October 2002 - January 2003 (Bonforte et al., 2007; Currenti et al., 2010; Alparone et al., 2012). A critical question was whether the seismic activity could have been viewed as a signature of volcanic unrest in the northern sector. Carrying out a 3D numerical modeling inversion of deformation data encompassing the seismic event, Currenti et al. (2010) evidenced the active tensile loading exerted by the attempt of a magmatic intrusion in the upper part of the fault system. Therefore, this event, which was a response to the initial forming intrusion, provided insights into a possible interaction between pre-eruptive magmatic intrusion and subsequent loading and rupture of the PFS.

On more other occasions, however, the earthquakes were not followed by any ensuing volcanic unrest (Bonaccorso et al., 2012). The latest intense seismic swarm took place on 2-3 April 2010 and caused coseismic surface faulting and severe damages to tourist resorts and villages close to the PFS structure (Guglielmino et al., 2011). Subsequently, explosions and ash emissions occurred at the summit craters on 7-8 April. These events raised the alert level for the volcanic and seismic hazard related to an impending flank eruption in the northern sector of the volcano, similar to what happened before the 2002-2003 eruption. Therefore, the question to be addressed is whether the seismic swarm was a possible response to accommodate the stress change induced by possible magma intrusions and, consequently, a fingerprint of an impending eruption. In fact, no volcanic unrest occurred in the following months.

To investigate the behavior of the PFS during the 2-3 April 2010 seismic swarm, we carried out a detailed study of the fault kinematics by inversion of ground deformation data. The analysis and modeling of ground deformation data could shed light on the interaction between volcanic activity and seismicity in such a complex volcano-tectonic setting. Differential Synthetic Aperture Radar (SAR) Interferometry (DInSAR) (Gabriel et al., 1989; Massonnet et al., 1993) has made it possible detailed observations of surface deformation (Neri et al., 2009; Solaro et al., 2010; 2011), providing important constraints on active deformation sources. A preliminary estimation of the active sources of the April 2010 seismic event was performed in Guglielmino et al. (2011) by inverting a set of geodetic data from ground based stations (GPS and levelling) and satellite platforms (ENVISAT and ALOS satellites) and by using a model based on the analytical formulation of rectangular fault segments embedded in a homogeneous half-space (Okada, 1992).

We extend this analysis with the inclusion of data from the new-generation COSMO-SkyMed satellites, which could give further constraints thanks to the short (a few days) revisiting times and the high spatial resolution (about 3 m). The availability of SAR datasets from different platforms allows us to compare the estimated displacement fields and to derive a high-resolution model for the slip distribution along the PFS. The integration of different satellite data and the construction of a more realistic model give us the opportunity to discriminate the mechanism responsible for the PFS seismic activation during the April 2010 seismic swarm. More generally, the inferences derived from geodetic inversions improve our understanding of the relationship between volcanic unrest at Etna and seismic activation along the PFS, providing useful implications for eruptive activity prediction and volcano hazard assessment.

2. M4.3 earthquake rupture along the Pernicana Fault System

The PFS is one of the most outstanding and active tectonic structures of Mt Etna and delineates the northern margin of the volcano's sliding flank, as confirmed by geological, seismological and geophysical investigations (Neri et al., 2004; Azzaro et al., 2001; Bonforte et al., 2007). It develops eastward from the North East Rift (from 1850 m a.s.l.) to the coastline, over a distance of about 18 km (Acocella and Neri et al., 2005), constituting a left-lateral transcurrent zone that cuts across the northeastern flank of the volcano (Tibaldi and Groppelli 2002). The PFS, composed of discrete segments arranged in a right stepping en-èchelon configuration and of a near continuous left lateral shear zone, shows a very high slip-rate of about 2 cm/year, mainly related to the sliding of the eastern flank of the volcano (Lo Giudice and Rasà, 1992; Azzaro et al., 2001; Bonforte et al., 2007, Ruch et al., 2010). In the upper part of the PFS, which is often intruded by magma, tensile rupture mechanisms prevail, while normal/strike-slip characterizes the intermediate zone and pure strike-slip the easternmost shallow part. Earthquakes related to this structure, which are characterized by small to moderate magnitude (< 4.5 Ml) and by shallow hypocentral area (about 2-4 km), mainly affect the western and central segments while the lower eastern segment is characterized by an aseismic fault movement (Azzaro et al., 2001). The widespread seismicity, which characterizes the western and central segments of the fault, confirms that the structure is highly active (Bonforte et al., 2007). Sometimes the PFS has been seismically active immediately before the onset of an eruption and within the first week of volcanic activity at the nearby NE Rift (Neri et al., 1991; Garduno et al., 1997; Tibaldi and Groppelli, 2002; Acocella and Neri, 2003; Acocella et al., 2003; Currenti et al., 2008). On the other hand, there were long periods (i.e. 1984-1988) during which the PFS has shown continuous activity, but no eruptions occurred from the NE Rift (Azzaro et al., 1988; Acocella and Neri, 2005). After the 2002-03 eruption, which was preceded by a M3.7 event (Table 1), a marked acceleration of the eastern motion of the PFS was observed. Over the last years, a strong increase of seismicity, also characterized by swarms, was recorded by INGV-CT permanent local seismic network close to the Pernicana Fault (Alparone et al., 2009). The last intense seismic release started along the fault on 2 April 2010 at 19:06 (GMT). About 170 events were recorded until 07:42 of 3 April , accompanied by ground fracturing with left lateral movement of about 0.5 m. The largest event occurred at 20:04 on 2 April 2010 with a magnitude of Ml 4.3 at a depth of 300 m b.s.l. (Table 1). At the beginning, the earthquakes affected the central sector of the PFS (Fig. 1), at a depth of about 1000 m b.s.l. and successively moved westwards approaching the NE Rift (Langer, 2010).

3. DInSAR data analysis

We investigated the displacement induced by the 2-3 April 2010 seismic events by means of InSAR data acquired over the volcano using the Cosmo-SkyMed (CSK) and ALOS radar systems. A set of 66 CSK images acquired with a look angle around 56 deg on descending orbits between September 2009 and September 2010 was considered; in addition, one ALOS couple acquired with a look angle of about 38 deg on an ascending orbit was also used in this study.

The CSK differential interferogram with the shortest available time span across the event, i.e., the one involving the acquisitions on 30 March 2010 and 7 April 2010, was computed shortly after the event (Italian Space Agency, 2011) and is shown (in radar coordinates) in Fig. 2a. The white line represents the known trace of the PFS. It is evident that in a narrow area surrounding the middle part of the fault, the interferogram is affected by a strong decorrelation noise that severely corrupts the computed phase (Zebker and Villasenor, 1992). This is most probably due to the temporal decorrelation induced by the heavy vegetation covering the area, which is particularly relevant for X-band radar systems. In fact, large decorrelated areas have been observed also in short time interferograms not including the earthquake. In addition to this effect, a low spatial frequency fringe pattern that mimics a typical seismic signal is also observed. However, both leveling campaigns and other independent satellite observations (Guglielmino et al., 2011) indicate that the deformation associated with the earthquake should rapidly decrease away from the fault trace, thus suggesting the presence of a significant contribution related to atmospheric effects (Goldstein, 1995) in the interferogram.

To capture the possible small scale deformation associated with the earthquake, we take advantage of the high resolution capability of CSK data. Fig. 2b shows a zoom in the area indicated by the dashed rectangle in Fig. 2a at the full sensor resolution (about 3m x 3m). This underlines that a large and very concentrated deformation signal is present in the eastern part of the area (indicated by the black arrow), very close to the fault trace. Due to its limited spatial extension, this deformation pattern is not visible at a lower resolution, thus making the use of CSK data a unique opportunity to study this phenomenon with more details.

In addition to single interferogram analysis, multiple acquisition approaches, exploiting a large number of data acquired on the same satellite orbit (Sansosti et al., 2010), can be used to further characterize the phenomenon and to separate noises from the useful signal. We first applied a stacking technique (Peltzer et al., 2001) aimed essentially at calculating the average of all the cumulative displacements computed from each single full resolution interferograms covering the event. To reduce both the temporal and spatial decorrelation effects, we used only the interferograms characterized by a short temporal interval (temporal baseline) and a short orbital separation (spatial baseline) between the interferometric SAR image couples. The full range (unwrapped) phase was computed by using the Minimum Cost Flow phase unwrapping algorithm (Costantini and Rosen, 1999). Obviously, in this case, the stacking approach relies on the hypothesis that no event, other than the earthquake, occurred in the considered time interval, which is verified later on in this section. For this reason, we restricted the time period considered for stacking to a few months (except for one data pair), thus selecting the 7 interferograms reported in Table 2. The obtained cumulative displacement, shown in Fig. 2c for the same area of Fig. 2a, highlights that the deformation is concentrated around the fault and a significant part of the atmospheric signal has been reduced.

As an additional analysis, we also applied a full resolution implementation of the Small BAseline Subset (SBAS) approach (Berardino et al., 2002) to all the available 66 CSK data acquired on the same descending orbit covering almost one year (from September 2009 to September 2010). To limit the computational load, we processed only data associated with the small area delimited by the white box in Fig 2c. In this case, we applied the Extended Minimum Cost Flow Phase Unwrapping procedure (Pepe et al., 2011), which allows the generation of full resolution deformation time series through the SBAS approach. This technique is particularly appropriate for non-linear signals (as those expected for a seismic event) since it does not rely on any linear model assumption to compute the time series and it exploits the SBAS inversion directly on the full resolution DInSAR unwrapped interferograms, without using the corresponding multilook phase sequences, as in Lanari et. al. (2004).

The obtained cumulative ground deformation is shown in Fig. 2d and substantially confirms the results of the stacking procedure. However, the use of a larger number of images improves the atmospheric filtering operation. The atmospheric noise presents a strong correlation in space, but it is poorly correlated in time, thus a spectral filtering in time can be implemented to detect and cancel out the noise (Ferretti et al., 2000; Berardino et al., 2002). However, the filtering procedure must be carefully adapted whenever seismic signals are involved in order not to impair possible true discontinuities present in the data and associated with the seismic event. In fact, to separate components of seismic signal and atmospheric noise in the time domain, instead of using a classical low pass strategy, we used a median filtering that has the peculiarity to preserve discontinuities while reducing the noise (Niedzwiecki and Sethares, 1995).

The plot in Fig. 2e shows the displacement time series (projected onto the line of sight) for the corresponding area indicated in Fig. 2d. The time series shows a clear jump in correspondence to the date of the earthquake, while no other sharp variations before and after the event are evident, thus indicating that, apart from the earthquake, no other significant event occurred in the considered area during the investigated period (mid 2009 - end of 2010). This also validates the hypothesis that allowed us to compute the deformation map shown in Fig 2c via the stacking approach.

However, the maximum LOS displacement observed by CSK is about 5 cm, which is smaller than 8 cm and up to 37 cm for vertical and East-West components, respectively, as reported in Guglielmino et al. (2011). Horizontal ground displacements of the order of 30 cm have also been observed during field trips (Neri, personal communication). These data do not match CSK measurements, even considering possible compensation of horizontal and vertical components of the displacement due to the projection onto the line of sight. This is because the area of maximum deformation falls within the decorrelated area where CSK, which operates at X-band (wavelength 3.1 cm), is unable to provide any measurement, being the coherent pixels essentially limited to the areas covered by lava.

To circumvent this problem, we complement the above discussed deformation information with that obtained by processing SAR data acquired by the ALOS radar system that operates in L-band with a larger wavelength (23.6 cm) and, therefore, is less affected by decorrelation phenomena, especially in vegetated terrains such as in the PFS area. One ALOS differential interferogram (22 March 2010 - 7 May 2010) was computed (Fig. 3a). The maximum detectable deformation in the direction of satellite line of sight (LOS) is about 23 cm, corresponding approximately to two fringes in the interferogram, in agreement with previous analysis based on the same data (Guglielmino et al., 2011) and on field campaign information (Neri, personal communication). In this case, the lack of a sufficiently large number of ALOS acquisition on the same track prevented us from generating deformation time series via the SBAS approach; however, other ALOS interferograms generated with independent acquisition show a similar deformation pattern, thus confirming that the observed signal is related to the actual deformation rather than atmospheric noise (Guglielmino et al., 2011). The ALOS differential interferogram has been unwrapped by using the Minimum Cost Flow (MCF) approach (Costantini and Rosen, 1999). The corresponding deformation map is shown in Fig. 3b and has been used, jointly with the computed CSK displacement map (Fig. 2c), to model the deformation source.

The joint use of both CSK and ALOS data gives us complementary information about the occurred ground changes. Full spatial coverage of the ALOS interferogram allows understanding that the displacements are confined in a very narrow area nearby the PFS and exponentially decay moving away from the fault trace (Fig. 3). On the other hand, CSK data allow analyzing the displacement field with a greater detail (Fig. 2b and 2d). However, the smaller operational wavelength of CSK data introduces more significant decorrelation noise in the interferograms (Zebker and Villasenor, 1992), thus reducing the spatial coverage. Accordingly, the combined use of ALOS and CSK data allows us to retrieve the whole deformation pattern with an overall satisfactory level of detail.

4. Slip distribution models

An interpretation of the co-seismic displacements due to the April 2010 seismic swarm was recently proposed in Guglielmino et al., (2011) using the analytical solution for rectangular dislocations (Okada, 1992). However, the computed displacement magnitudes and spatial distributions show a limited consistency with the satellite and in situ ground deformation data, which may be related to the simplified fault geometry and the uniform-slip assumption. The gaps and overlaps between the assumed rectangular dislocation sources induced strain concentrations at the source edges (Meade, 2007), which are not in agreement with the observed deformation pattern. Starting from these results, we investigated how the model can be improved for a more accurate estimation of the movements of the PFS in a realistic description of the fault slip distribution from the joint inversion of deformation data acquired by both the new generation X-band SAR sensors onboard the COSMO-SkyMed satellites and the L-band sensor of ALOS. The inversion procedure is composed of three main steps (Currenti et al., 2010; 2011): (i) meshing the computational domain and subdividing the fault surface in a finite number of elements; (ii) computing the Green's functions for static displacements caused by unit slip over each element; and (iii) solving an inversion problem constrained by geodetic data to determine the slip distribution.

The observed ground displacements well evidence the marked dislocation across the fault trace, which is in good agreement with field mapping of surface ruptures and traces from high resolution DEM. This constrains the length (along-strike dimension) and strike of the fault segments on the ground well. To account for its spatial complexity, the fault rupture is closely approximated by a curved line composed of 16 segments of about 400 m length longitudinally extended from 504 to 510 km eastward, where the main deformation pattern is observed (Figs. 2 and 3). Over the last decade, the integration of multiple data sets such as mapped surface ruptures, high-precision seismic locations (Alparone et al., 2009), results of geodetic inversions for a simplified fault geometry (Bonforte et al., 2007; Currenti et al., 2010; Guglielmino et al., 2011) have well defined the geometry of the PFS and, hence, we adopt a fixed fault geometry. However, because of the non-planar geometry of the PFS, we represented the fault system as a set of quadrangles, which better adapt to its complex geometry. Discretization of surfaces into quadrangular elements allows the construction of three-dimensional fault surfaces that more closely approximate curviplanar surfaces and curved tiplines, consistent with the full extent of available data. Considering that the main seismogenic volume of the PFS extends at depth for few kilometers, we discretized the fault surface from the free surface to 1500 m in depth. Using the LaGriT (2010) meshing software, we discretized the fault surface into sub-quadrangles, whose size increases with depth to provide a more uniform resolution of slip among quadrangles at different depth (Simons et al., 2002). Given that the deformation pattern is quite narrow, the spatial resolution of the discretization has to be very high. We subdivided the fault surface into 592 quadrangles, whose sizes increase with depth. Using a quadtree resampling algorithm, we obtained quadrangles whose larger size varies from 100 m near the surface to 400 m at greater depth. The computation of the Green's function of each quadrangle is performed as the sum of the Green's functions for the two triangles composing each quadrangle, thus implementing the analytical solution devised by Meade (2007) for triangular dislocations embedded in a homogeneous elastic half-space. The DInSAR data (Figs. 2c and 3b), which provide a dense spatial resolution able to ensure a robust inversion, were used to find the slip in each patch by means of a Quadratic Programming (QP) algorithm with bound and smoothening constraints based on the second-order spatial derivative to suppress slip oscillations (Currenti et al., 2010). In order to limit the computational burden in the modeling inversion, the number of DInSAR observations from both ALOS and CSK satellites was reduced. Since the deformation rapidly decreases within about 500 m from the PFS trace (Fig. 4c), we implemented a sub-sampling procedure of the displacement points on the basis of the distance from the fault, ending up with a final dataset of 761 points for CSK and 1822 points for ALOS (Fig. 4a-b). Note that, despite the higher resolution of the CSK sensor, the number of usable ALOS points is sensibly higher than the CSK one because the latter sensor is drastically limited by the decorrelation phenomenon affecting the X-band data. In addition to SAR data, also the leveling data recorded at 19 benchmarks during two surveys carried out in November 2009 and April 2010 along the Pernicana levelling route (Guglielmino et al., 2011) were included in the inversion process. Since CSK deformation time series show that no other significant deformative episode occurs in the time period covered by the data (Figs. 2d-e), we can easily assume that all the available geodetic data basically capture the deformation related to the earthquake only.

As multiple datasets are used to constrain the model, the inversion account for errors by weighting the data misfit using a matrix of data weights in order to give each data set its influence over the slip estimates. We used a diagonal matrix containing the inverse of the standard deviation of the data. The estimated errors (standard deviation) were half a fringe for the DInSAR and 1 $mm/km^{1/2}$ for the levelling data, respectively (Currenti et al., 2010; Guglielmino et al., 2011).

We imposed a left-lateral strike-slip and normal dip-slip constraints to the solution in agreement with the historical activity of the fault (Azzaro et al., 2001), thus formalizing an inversion problem with 1184 unknowns on the strike and dip slip components. The deformation patterns (projected along the LOS) computed from the best-fitting model and the corresponding residuals with respect to the observed data are shown in Fig. 5a-d. The deformation measured by DInSAR data, both from CSK and ALOS satellites, are well predicted by the retrieved model (Fig. 5a-b), with residuals within the error range of the used DInSAR technique over most of the covered area (Fig. 5c-d). The Root Mean Square Error (RMSE) of the residual is 2.1 cm for ALOS and 0.9 cm for CSK data, accordingly to the higher sensitivity of CSK data and to the use of stacked displacement image that reduces the atmospheric errors. Moreover, thanks to the high resolution of the proposed model, the leveling data are also well reproduced despite the high deformation gradient along the fault. A comparison between the deformation predicted by the model and that measured at the levelling benchmarks is shown in Fig. 5e. The slip distribution model obtained with the joint inversion of all the available geodetic data is shown in Fig. 6.

We find that the combination of strike and dip slip on the PFS well reproduces the near-fault deformation pattern. If a combination of the strike-slip, dip-slip, and tensile components is taken into account, the results show a similar fit to the data. The RMSE between the data and the model predictions slightly decreases to 1.9 cm for ALOS and 0.8 cm for CSK. Moreover, the amplitude of the tensile component is found to be negligible with respect to the strike-slip and dip–slip components, confirming the dominant mode of the fault. Integrating the slip over the fault area and using an average shear rigidity modulus of 1 GPa for the shallow layers, we obtained an estimate of the geodetic moment (Santini et al., 2004) on the order of 1×10^{15} Nm associated with a magnitude of Ml 3.9

5. Discussion

The space geodetic observations provide robust constraints on the spatial extent and amount of the earthquake-induced displacements within the PFS fault zone. The resulting inversion, based on both SAR and levelling data, shows that the model, closely describing the geometry of the surface ruptures, yields good fit to the geodetic data. Using variable strike and dip slip over the fault, the geodetic inversion indicates that the fault is characterized by a prevailing left-lateral and normal dip-slip motion. The numerical model shows a predominant strike-slip concentrated in a very shallow layer, decaying within 500 m from the free surface (Fig. 6a). The major strike-slip component, with a maximum of about 0.4 m, is in correspondence to the epicenter of the most energetic seismic event (Ml 4.3) recorded during the swarm, with a longitudinally elongated extension of about 2 km. The amplitude of the normal dip-slip component reaches a maximum of about 0.3 m and is also concentrated in a shallow layer (Fig. 6b). A gap between the activated areas is observed, where a deficit in the dip-slip occurs. This could be ascribed to the morphological change in the strike of the fault trace, which could have played as a barrier to the eastward slipping as observed in the deformation pattern (Fig. 4a).

Of particular interest is the absence of significant deformation in the western part of the PFS, where the seismic swarm migrated, and the apparent deficit of slip at the depth of the most energetic events. This leads us to suppose that the intense rupture occurred in the very shallow layers characterized by reduced strength properties, as confirmed by the low QP values, derived from seismic tomography attenuation analysis (Barberi et al., 2010), indicative to the high degree of cracking along the PFS. The extent of this compliant zone seems to be very shallow (less than 500 m deep), in which a strong reduction of effective elastic moduli can be expected and interpreted in terms of changes in the micro-crack density or the effective damage parameters. Slip is, however, also affected by several other factors such as structural heterogeneity, friction and fault rheology, and the past activity of the fault.

The model results give also evidence that no fault-normal dilation, neither shallow nor deep, is required to explain the observed deformation data. Therefore, no significant volume changes are found along the fault surface. Moreover, no significant deformation changes were detected in the summit area, excluding the presence of other active deformation sources from magmatic activity. This suggests that no tensile actions were exerted, and, hence, rules out the involvement of magmatic intrusions in the summit area or in the north-eastern flank, as possible trigger mechanisms for the seismic swarm. These results provide a completely different scenario from that derived for the 22 September 2002 M3.7 earthquake, where the co-seismic shear-rupture that took place along the PFS was accompanied by a tensile mechanism associated with a first attempt of magma intrusion that preceded the lateral eruption occurred here a month later (Currenti et al., 2010). Indeed, the spatio-temporal evolution of the seismic pattern (migrating from east toward west) further supports the assumption that for the 2-3 April 2010 events the most likely mechanism responsible for the PFS seismic activation derives from the tectonic loading, possibly associated with the eastern flank sliding of the volcano edifice (Ruch et al., 2010). The acceleration of the flank sliding recorded since 2002 (Bonaccorso et al., 2006) could have significantly loaded the PFS, intensifying the occurrence of seismic activity in the last years (Alparone et al., 2009).

6. Conclusive Remarks

SAR and leveling data combined with a high-resolution modeling inversion have proven to be useful for giving a complete picture of the 2-3 April 2010 seismic swarm at Etna. CSK data offered the quickest possibility to image the fault rupture within a few days of the earthquake (Italian Space Agency, 2011). However, it was difficult to constrain the fault geometry using CSK data only, because the X-band radar data are affected by decorrelation noise mostly related to the strong vegetation of the PFS area. In order to amend this disadvantage of the CSK data, we also used one available ALOS data pair covering the footwall of the PFS to constrain the fault model. Leveling data, acquired at sparsely-distributed locations before and after the earthquake, were also used to constrain the frames of InSAR observations.

The increasing quality and quantity of InSAR data available in terms of spatial and temporal resolution were fully exploited in the slip-inversion procedure, capturing the deformation pattern and identifying the mechanism responsible for the PFS seismic activation. The flexibility of the method permitted the construction of a fault model with curved three-dimensional surfaces, which accounts for the fault surface trace. The fitting of our distributed-slip model to the observed data is dramatically improved with respect to uniform slip models, especially for the near-field measurements accompanying the seismic swarm. The slip distribution pattern allowed us to quantify the kinematics of the PFS and documented the absence of new magmatic intrusion in the north-eastern flank.

Summing up, our results elucidated the mechanisms responsible for earthquake ruptures occurring along the PFS. The 2002 and 2010 case studies are representative of the two main possible causes triggering the PFS seismicity. Similar seismic releases can be produced along the PFS by magma intrusion attempts leading to eruptions (2002 case) or flank sliding stretching the eastern sector of Mt Etna (2010 case). Establishing the relationship between volcanic unrest at Etna and PFS seismic activation, therefore, is critical to understanding Etna mechanical behavior, and could be important in forecasting future lateral eruptions.

More generally, the dense pattern of ground deformation, provided by integration of data from different satellites, together with refined modeling for fault slip distribution enables a comprehensive understanding of the kinematics across the different volcano sectors marked by active fault systems subjected to seismic or aseismic deformation. In volcanoes where the activity is controlled by volcano-tectonic interaction processes, such as Chaiten (Wicks et al, 2011), Kilauea (Brooks et al., 2008; Montgomery-Brown et al., 2010), Sierra Negra (Jonsson, 2009) and Arenal (Ebmeier et al., 2010), the data flow provided by COSMO-SkyMed satellites and the upcoming Sentinel-1 mission at short revisiting time will contribute to a timely evaluation of the ongoing seismic activity and, thus, also to a forecasting of impending hazards.

ACKNOWLEDGMENTS

This work has been partially supported by the Italian Space Agency (ASI) through the SAR4Volcanoes project under the agreement I/034/11/0. The seismic events were available from the catalogue of the Istituto Nazionale di Geofisica e Vulcanologia – Sezione di Catania at the website http://www.ct.ingv.it/ufs/analisti. Comments by Editor Marvin Bauer and three anonymous reviewers greatly improved the manuscript.

References

Acocella, V., Behncke, B., Neri, M., D'Amico, S., 2003. Link between large-scale flank slip and 2002–2003 eruption at Mt. Etna (Italy). Geophysical Research Letters 30 (24), 2286.

Acocella, V., Neri, M., 2003. What makes flank eruptions? The 2001 Mount Etna eruption and its possible triggering mechanisms. Bulletin of Volcanology 65, 517–529.

Acocella V Neri M., (2005) Structural features of an active strike-slip fault on the sliding flank of Mt Etna (Italy). J. Strtuct. Geol. 27, 343-355.

Alparone, S., Gambino, S., Mostaccio, A., Spampinato, S., Tuvè, T., Ursino A., (2009), Structural features of the Pernicana Fault (M. Etna, Sicily, Italy) inferred by high precise location of the microseismicity, Geophysical Research Abstracts, 11, EGU2009-8171, EGU General Assembly 2009.

Alparone, S., O. Cocina, S. Gambino, A. Mostaccio, S. Spampinato, T. Tuvè, A. Ursino (2012), Seismological features of the Pernicana–Provenzana Fault System (Mt. Etna, Italy) and implications for the dynamics of northeastern flank of the volcano, J. Volcanol. Geotherm. Res., doi:10.1016/j.jvolgeores.2012.03.010

Azzaro R, Ferrelli L, Michetti AM, Serva L, Vittori E (1998) Environmental hazard of capable faults: the case of the Pernicana Fault (Mt. Etna, Sicily). Nat Hazards 17, 147–162

Azzaro R, Mattia M, Puglisi G (2001) Dynamics of fault creep and kinematics of the eastern segment of the Pernicana fault (Mt. Etna, Sicily) derived from geodetic observations and their tectonic significance. Tectonophys 333,401–415.

Azzaro, R., D'Amico, S., Mostaccio, A., Scarfì, L. and Tuvè, T. (2006): Terremoti con effetti macrosismici in Sicilia orientale nel periodo Gennaio 2002 - Dicembre 2005. Quad. Geof., 41.

Barberi G., Cocina O., Giampiccolo E., Patané D., Zuccarello L., (2010) Advances in the VT earthquakes locations by new structural models at Mt. Etna obtained by using velocity and attenuation tomographies, In: The VOLUME Project – VOLcanoes: Understanding subsurface mass movement (C.J. Bean, A.K. Braiden, I. Lokmer, F. Martini e G.S. O'Brien, ed.), pp. 106-117, ISBN: 978-1-905254-39-2.

Berardino, P., G. Fornaro, R. Lanari, and E. Sansosti (2002), A new algorithm for surface deformation monitoring based on small baseline differential SAR interferograms, IEEE Trans. Geosci. Remote Sens., 40, 2375–2383, doi:10.1109/TGRS.2002.803792.

Bonforte, A., S. Gambino, F. Guglielmino, F. Obrizzo, M. Palano, and G. Puglisi (2007), Ground deformation modeling of flank dynamics prior to the 2002 eruption of Mt. Etna, Bull. Volcanol. 69, 757-768, doi: 10.1007/s00445-006-0106-1.

Bonaccorso, A., A. Bonforte, F. Guglielmino, M. Palano, and G. Puglisi (2006), Composite ground deformation pattern forerunning the 2004–2005 Mount Etna eruption, J. Geophys. Res., 111, B12207, doi:10.1029/2005JB004206.

Bonaccorso, A., G. Currenti, and C. Del Negro (2012), Interaction of volcano-tectonic fault with magma storage, intrusion and flank instability: A thirty years study at Mt. Etna volcano. J. Volcanol. Geotherm. Res., http://dx.doi.org/10.1016/j.bbr.2011.03.031.

Brooks, B. A., Foster, J., Sandwell, D., Wolfe, C. J., Okubo, P., Poland, M., Myer, D., (2008), Magmatically Triggered Slow Slip at Kilauea Volcano, Hawaii, Science, 321, 29, 1177.

Costantini, M. and P.A. Rosen, (1999), A generalized phase unwrapping approach for sparse data, Proceedings of International Geoscience and Remote Sensing Symposium 1999 (IGARSS'99), Hamburg, Germany, June 28–July 21, 267–269.

Currenti, G., A. Bonaccorso, C. Del Negro, F. Guglielmino, D. Scandura, and E. Boschi (2010), FEM-based inversion for heterogeneous fault mechanisms: application at Etna volcano by DInSAR data, *Geophys. J. Int.*, doi: 10.1111/j.1365-246X.2010.04769.x.

Currenti, G., C. Del Negro, G. Ganci, and C. Williams (2008), Static stress changes induced by the magmatic intrusions during the 2002–2003 Etna eruption, J. Geophys. Res., 113, B10206, doi:10.1029/2007JB005301.

Currenti, G., Napoli, R., Del Negro, C., (2011). Toward a realistic deformation model of the 2008 magmatic intrusion at Etna from combined DInSAR and GPS observations, Earth and Planetary Science Letters Earth and Planetary Science Letters, 312, 22–27, DOI 10.1016/j.epsl.2011.09.058.

Ebmeier, S. K., J. Biggs, T. A. Mather, G. Wadge, and F. Amelung (2010), Steady downslope movement on the western flank of Arenal volcano, Costa Rica, Geochem. Geophys. Geosyst., 11, Q12004, doi:10.1029/2010GC003263.

Ferretti, A., C. Prati, and F. Rocca (2000), Nonlinear subsidence rate estimation using permanent scatterers in differential SAR interferometry, IEEE Trans. Geosci. Remote Sens., 38, 2202–2212, doi:10.1109/36.868878.

Gabriel, A. K., R. M. Goldstein, and H. A. Zebker (1989), Mapping small elevation changes over large areas: Differential interferometry, J. Geophys. Res., 94, 9183–9191, doi:10.1029/JB094iB07p09183.

Garduno, V.H., Neri, M., Pasquare`, G., Borgia, A., Tibaldi, A., (1997). Geology of the NE Rift of Mount Etna, Sicily (Italy). Acta Vulcanologica 9, 91–100.

Goldstein, R. (1995), Atmospheric limitation to repeat-track radar interferometry, Geophys. Res. Lett., 22, 2517-2520.

Guglielmino, F., Bignami, C., Bonforte, A., Briole, P., Obrizzo, F., Puglisi, G., Stramondo,S., Wegmüller, U., (2011) Analysis of satellite and in situ ground deformation data integrated by the SISTEM approach: The April 3, 2010 earthquake along the Pernicana fault (Mt. Etna - Italy) case study, Earth and Planetary Science Letters 312, 327–336, doi:10.1016/j.epsl.2011.10.028.

Italian Space Agency (ASI) (2011), COSMO-SkyMed trains its eyes on Etna, available online at http://www.asi.it/en/news_en/cosmoskymed_trains_its_eyes_on_etna.

Jónsson, S., (2009), Stress interaction between magma accumulation and trapdoor faulting on Sierra Negra volcano, Galápagos, Tectonophysics, 471, 36–44.

Lanari, R., O. Mora, M. Manunta, J. J. Mallorqui, P. Berardino, and E. Sansosti (2004), A small-baseline approach for investigating deformations on full-resolution differential SAR interferograms, IEEE Trans. Geosci. Remote Sens., 42, 1377–1386, doi:10.1109/TGRS.2004.828196.

Langer, H., 2010. Rapporto sull'attività sismica in Sicilia orientale. Settimana 29.03.2010 –04.04.2010, INGV internal report, http://www.ct.ingv.it/index.php?option=com_docman&task =doc_view&gid=1761&tmpl=component&format=raw&Itemid=3312010.

LaGriT, (2011) Los Alamos Grid Toolbox, Los Alamos National Laboratory, <http://lagrit.lanl.gov>.

Lo Giudice E, Rasà R (1992) Very shallow earthquakes and brittle deformation in active volcanic areas: the Etnean region as an example. Tectonophysics 202, 257–268

Massonnet, D., M. Rossi, C. Carmona, F. Ardagna, G. Peltzer, K. Feigl, and T. Rabaute (1993), The displacement field of the Landers earthquake mapped by radar interferometry, Nature, 364, 138–142, doi:10.1038/364138a0

Meade, B.J., (2007) Algorithms for the calculation of exact displacements, strains, and stresses for triangular dislocation elements in a uniform elastic half space, Computers & Geosciences 33, 1064–1075, doi:10.1016/j.cageo.2006.12.003.

Montgomery-Brown, E. K., D. Sinnett, M. Poland, P. Segall, T. Orr, H. Zebker, and A. Miklius, (2010). Geodetic evidence for en echelon dike emplacement and concurrent slow-slip and Kilauea volcano, Hawaii, 17 June 2007, J. Geophys Res., v. 115, B07405, doi:10.1029/2009JB006658.

Neri, M., Garduno, V.H., Pasquarè, G., Rasà, R., 1991. Studio strutturale e modello cinematico della Valle del Bove e del settore nord-orientale etneo. Acta Vulcanologica 1, 17–24.

Neri, M., Acocella, V., Behncke, B., 2004. The role of the Pernicana Fault System in the spreading ofMt.Etna (Italy) during the 2002–2003 eruption. Bulletin of Volcanology, 66, 417–430, doi: 10.1007/S00445-003-0322-X.

Neri, M., F. Casu, V. Acocella, G. Solaro, S. Pepe, P. Berardino, E. Sansosti, T. Caltabiano, P. Lundgren, and R. Lanari (2009), Deformation and eruptions at Mt. Etna (Italy): A lesson from 15 years of observations, Geophys. Res. Lett., 36, L02309, doi:10.1029/2008GL036151.

Niedzwiecki, M., and W. A. Sethares (1995), Smoothing of discontinuous signals: the competitive approach, IEEE Transactions on Signal Processing, 43, doi: 10.1109/78.365281.

Okada, Y. (1992), Internal deformation due to shear and tensile faults in a half-space, Bull. Seism. Soc. Am., 82, 1018-1040.

Pepe A, L. D. Euillades, M. Manunta, R. Lanari (2011), New Advances of the Extended Minimum Cost Flow Phase Unwrapping Algorithm for SBAS-DInSAR Analysis at Full Spatial Resolution, IEEE Trans. Geosci. Remote Sens., 49, 4062-4079.

Ruch, J., V. Acocella, F. Storti, M. Neri, S. Pepe, G. Solaro and E. Sansosti (2010), Detachment depth revealed by rollover deformation: An integrated approach at Mount Etna, Geophys. Res. Lett., 37, L16304, doi:10.1029/2010GL044131.

Santini, S. , P. Baldi, M. Dragoni, A. Piombo, S. Salvi, G. Spada, and S. Stramondo (2004), Monte Carlo Inversion of Dinsar Data for Dislocation Modeling: Application to the 1997 Umbria-Marche Seismic Sequence (Central Italy), Pure appl. geophys. 161, 817-838, doi: 10.1007/s00024-003-

2474-1.Simons, M., Fialko, Y. and Rivera, L., (2002) Coseismic Deformation from the 1999 Mw 7.1 Hector Mine, California, Earthquake as Inferred from InSAR and GPS Observations, Bulletin of the Seismological Society of America, 92, 4, 1390–1402.

Sansosti, E., F. Casu, M. Manzo, and R. Lanari (2010), Space-borne radar interferometry techniques for the generation of deformation time series: an advanced tool for Earth’s surface displacement analysis, Geophys. Res. Lett., 37, L20305, doi:10.1029/2010GL044379.

Solaro, G., V. Acocella, S. Pepe, J. Ruch, M. Neri, and E. Sansosti (2010), Anatomy of an unstable volcano from InSAR: Multiple processes affecting flank instability at Mt. Etna, 1994–2008, J. Geophys. Res., 115, B10405, doi:10.1029/2009JB000820.

Solaro, G., F. Casu, L. Paglia, A. Pepe, S. Pepe, E. Sansosti, P. Tizzani, and R. Lanari (2011), SBAS-DInSAR time series in the last eighteen years at Mt. Etna volcano (Italy), 2011 IEEE International Geoscience and Remote Sensing Symposium (IGARSS), 3891-3894, doi: 10.1109/IGARSS.2011.6050081.

Tibaldi A, Groppelli G (2002) Volcano-tectonic activity along structures of the unstable NE flank of Mt.Etna (Italy) and their possible origin. J Volcanol Geotherm Res 115:277–302.

Wicks, C., de la Llera, J.C., Lara, L.E. and Lowenstern, J. (2011), The role of dyking and fault control in the rapid onset of eruption at Chaite´n volcano, Chile, Nature, 478, doi:10.1038/nature10541.Zebker, H. A., and Villasenor J. (1992), Decorrelation in interferometric radar echoes, IEEE Trans. Geosci. Remote Sens., 30, 950–959, doi:10.1109/36.175330.

Table

Table 1 – Main parameters of the seismic events (http://www.ct.ingv.it/ufs/analisti; Azzaro et al., 2006).

Date	**Hour**	**Latitude [km]**	**Longitude [km]**	**Depth [km]**	**Ml**
22/09/2002	16:01	4184.292	505.897	2.8	3.7
02/04/2010	20:04	4183.517	506.955	0.3	4.3

Table 2 – COSMO-SkyMed Interferometric pairs used in the stacking procedure

Master [dd-mm-yyy]	**Slave [dd-mm-yyy]**	**Perpendicular Baseline [m]**
24-12-2009	07-04-2010	21.4
24-12-2009	03-12-2010	-160.7
15-03-2010	16-04-2010	84.6
22-03-2010	16-04-2010	224.4
30-03-2010	15-04-2010	152.2
31-03-2010	15-04-2010	41.5
31-03.2010	16-04-2010	513.5

Figure 1

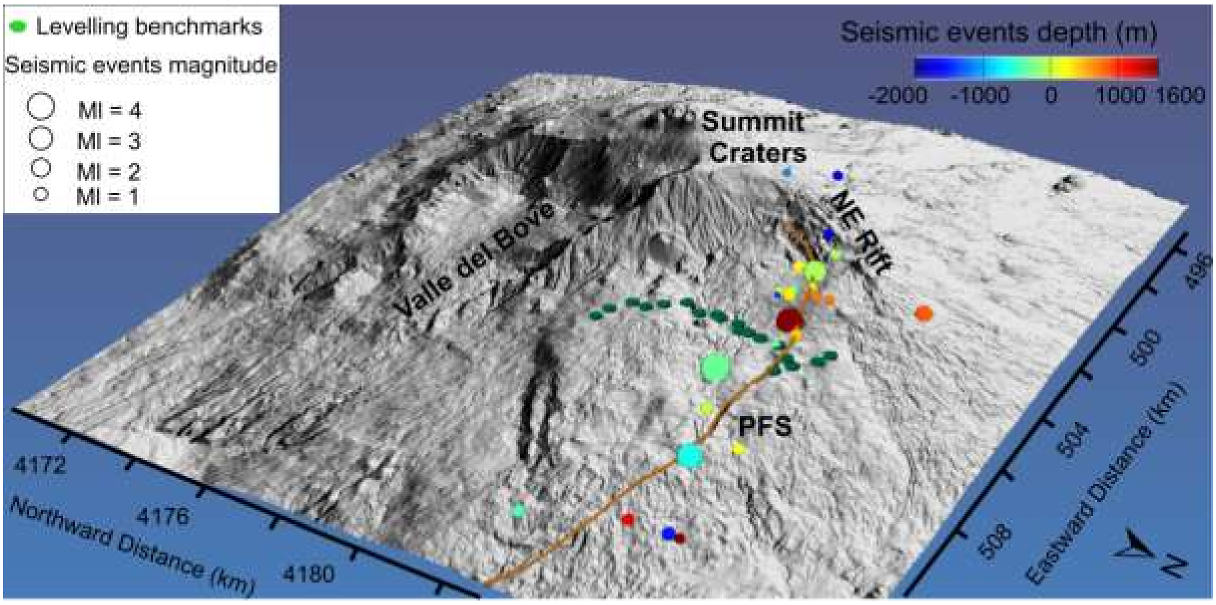

Figure 1 – 3D shaded relief map of Mt Etna with the structural lineament of the Pernicana Fault System (PFS) shown by brown line. The epicentres of the seismic events from 2 to 3 April 2010 are indicated by circles (http://www.ct.ingv.it/ufs/analisti). The levelling benchmarks (green circles) are also reported (from Guglielmino et al., 2011).

Figure 2

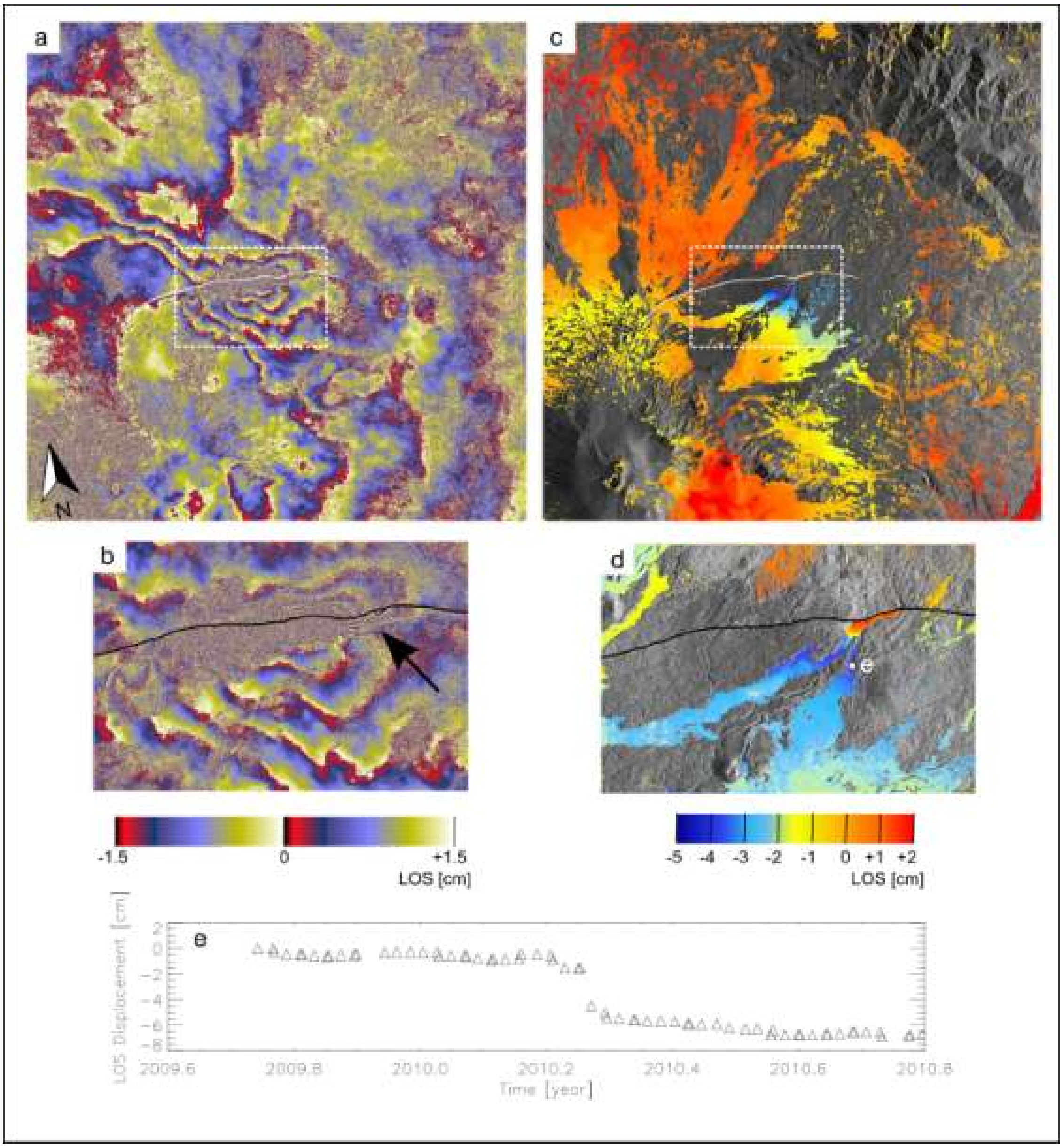

Figure 2 – (a) CSK differential interferogram in radar coordinates obtained with the data acquired along a descending orbit on 30 March 2010 and 7 April 2010. One fringe cycle corresponds to a displacement of about 1.5 cm; (b) zoom of the white box of the Fig. 2a: the interferogram is at the full resolution of the SAR sensor (3m x 3m); (c) cumulative displacement of the area of Fig. 2a obtained by applying the full resolution stacking procedure to the 7 interferograms covering the seismic event reported in Table 2; (d) cumulative displacement of the area of Fig. 2c obtained by applying the full resolution SBAS

processing to 66 CSK images acquired between 2009 and 2010; (e) deformation time series for the point e in Fig. 2d.

Figure 3

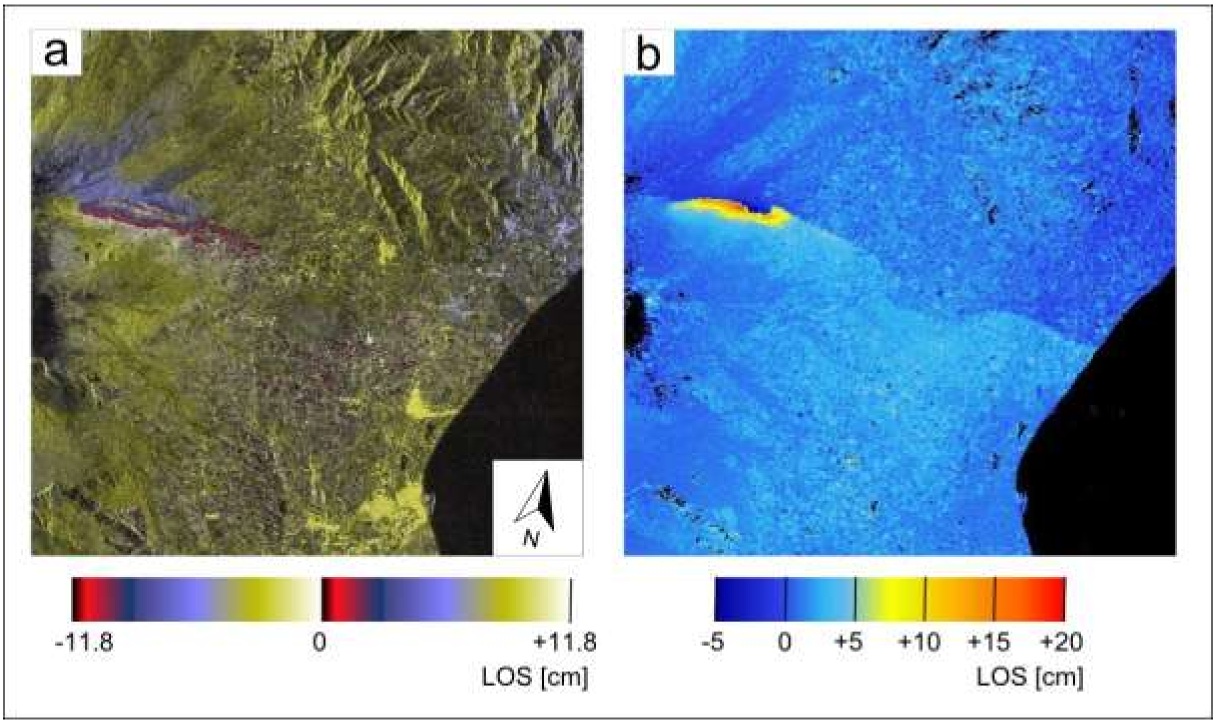

Figure 3 – (a) ALOS differential interferogram (in radar coordinates) superimposed on a SAR amplitude image. One fringe cycle corresponds to a displacement of about 11.8 cm. Acquisition dates are 22 March 2010 and 7 May 2010, i.e., one repeat cycle (46 days) covering the seismic event. (b) ground deformation map (in LOS) corresponding to the interferogram in (a).

Figure 4

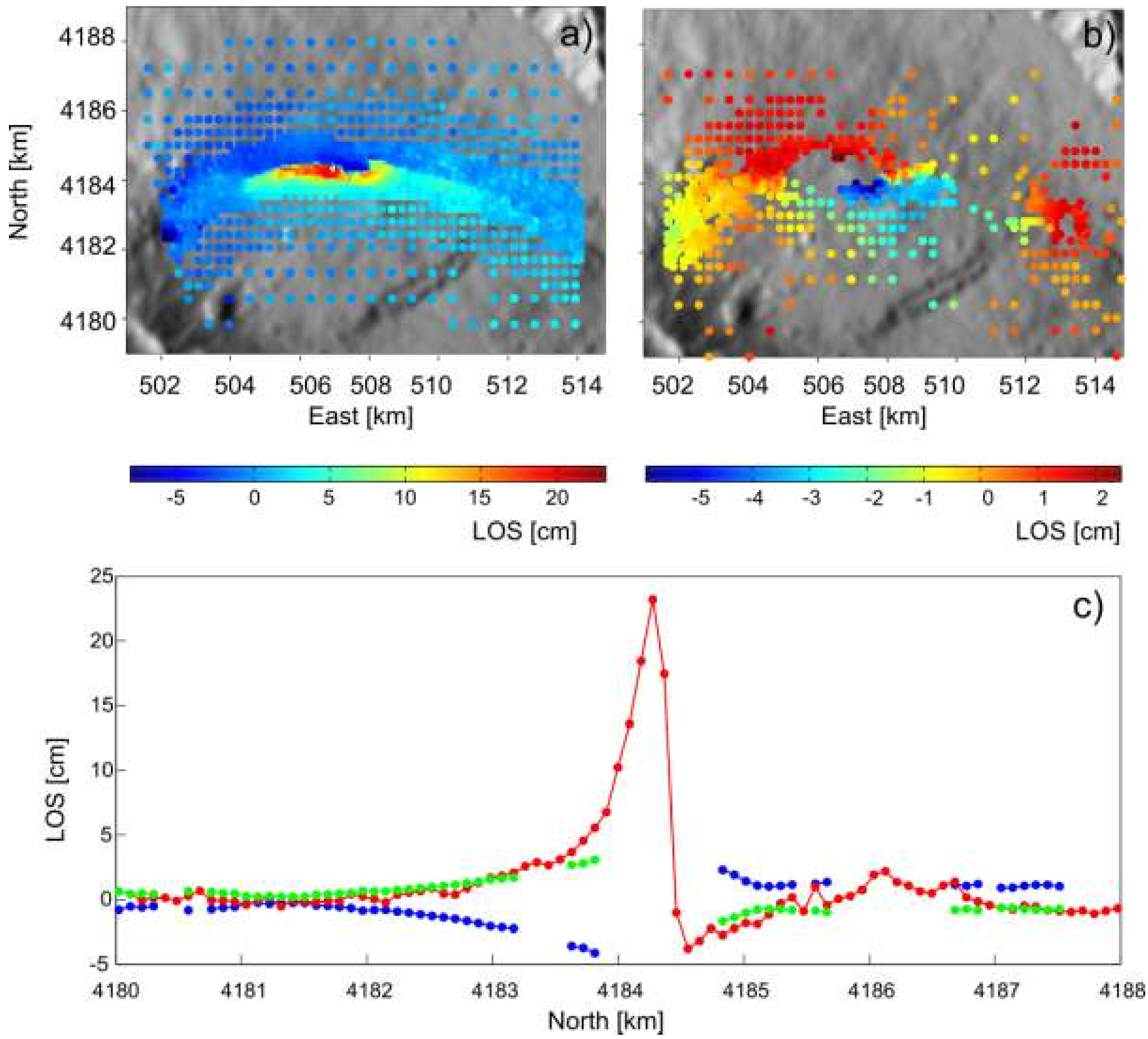

Figure 4 – Sampling of ALOS (a) and CSK (b) data. LOS displacements of ALOS (red line) and CSK (blue line) along the N-S profile centred at 506.8 km (c). Assuming that the displacement is almost EW, the CSK LOS displacement has been projected along the line of sight of ALOS (green line) to show the high agreement between the dataset from the two radar systems.

Figure 5

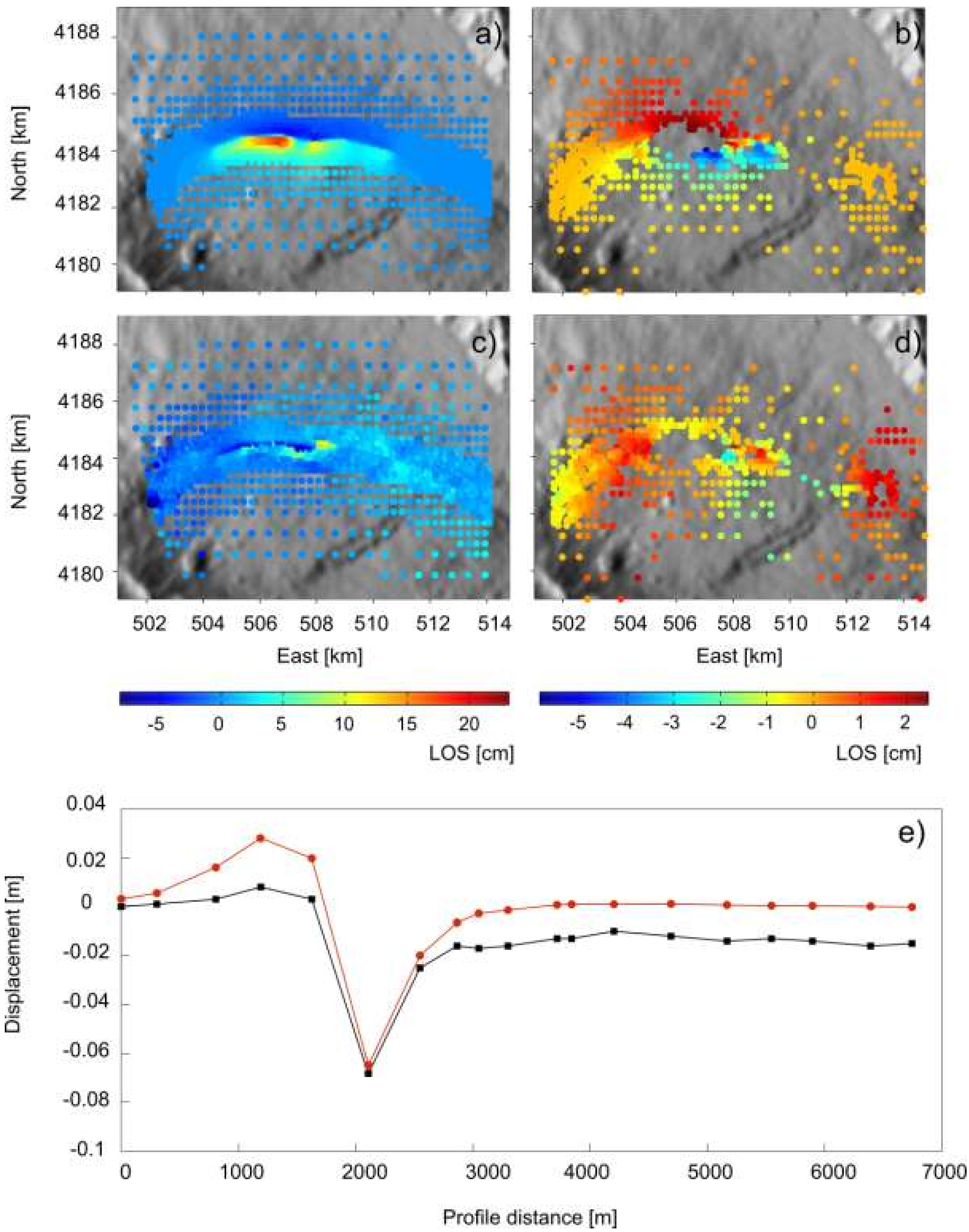

Figure 5 – Modeled and residual LOS displacements for ALOS (a, c) and CSK (b, d). Observed (black line; from Guglielmino et al., 2011) and computed (red line) vertical displacement at the levelling benchmarks (e).

Figure 6

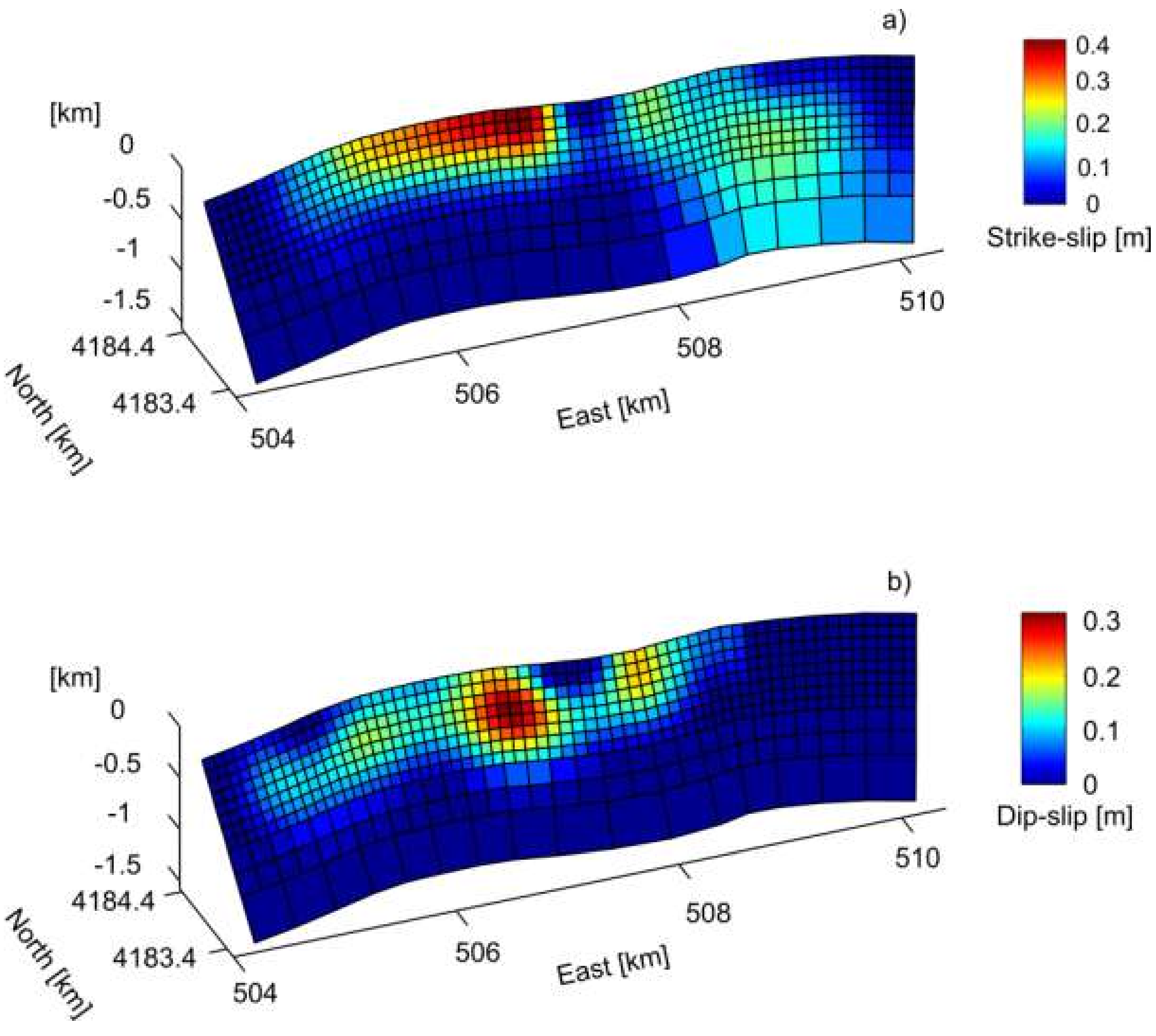

Figure 6 - Slip distributions along the PFS: (a) strike-slip (positive for left-lateral movement) and (b) dip-slip (positive for normal movement) components.